# Restructuring of Aggregates and Their Primary Particle Size Distribution During Sintering

**Maximilian L. Eggersdorfer and Sotiris E. Pratsinis**
Particle Technology Laboratory, Institute of Process Engineering, Dept. of Mechanical and Process Engineering, ETH Zurich, Zürich CH-8092, Switzerland

*DOI 10.1002/aic.14043*
*Published online February 25, 2013 in Wiley Online Library (wileyonlinelibrary.com)*

*During sintering (coalescence) of aggregates of polydisperse primary particles (PPs), restructuring takes place, the average PP size increases and the PP size distribution (PPSD) narrows affecting particle performance in a number of applications. Here, aggregate sintering by viscous flow, lattice, and grain boundary diffusion is simulated by multiparticle discrete element methods focusing on PP growth dynamics and elucidating the detailed restructuring of aggregates during their coalescence. The effect of initial PPSD and sintering mechanisms on the evolution of PP polydispersity (geometric standard deviation) and surface area mean diameter are presented. Each sintering mechanism results in a distinct evolution of PPSD but quite similar growth in average PP diameter. Grain boundary diffusion has the strongest impact among all sintering mechanisms and rapidly results in the narrowest PPSD, as it has the strongest dependence on PP size. During sintering of aggregates with initially monodisperse PPs, the PPSD goes through a maximum width before narrowing again as PPs coalesce. A power law holds between projected aggregate surface area and number of PPs regardless of sintering mechanism and initial PP polydispersity. This law can be readily used in aerosol reactor design and for characterization of aggregates independent of material composition, initial PP polydispersity, and sintering mechanism.*  *AIChE J*, 59: 1118–1126, 2013
*Keywords: agglomerate, grain boundary diffusion, lattice diffusion, primary particle size distribution, sintering, viscous flow*

## Introduction

Particle suspensions and films often exhibit unique properties that depend on particle-size distribution, like the opacity of titania pigments,[1] the color of quantum dot[2] or plasmonic[3] nanoparticle suspensions, and the superparamagnetism of iron oxide nanoparticles[4] to name a few. Typically, a narrow size distribution facilitates harvesting these effects from paints to solar cells,[5] biosensors,[6] and light-emitting devices.[7]

Aerosol processes allow rapid and scalable production of nanoparticles over a wide range of sizes.[8] In such processes, however, particles grow typically by Brownian coagulation that places a lower limit to the width of the size distribution, the so-called self-preserving size distribution[9] with a geometric standard deviation of about 1.45.[10] Such a constraint would limit aerosol-made particles in applications requiring narrow size distributions. Furthermore, when primary particles (PPs) with different high-temperature residence time histories (e.g., from different reactor streamlines[11] or reaction rates[10]) are mixed, fractal-like particles with quite polydisperse PP size distribution (PPSD) are obtained. This polydispersity, however, can be reduced by PP sintering (or coalescence) that proceeds inversely proportional to particle size, similar to condensation[12] that is routinely used in generation of monodisperse aerosols.

Correspondence concerning this article should be addressed to S. E. Pratsinis at pratsinis@ptl.mavt.ethz.ch.



Sintering can lead to a narrower size distribution of PPs than their parent aggregates.[13] The narrowest PPSD was obtained when $TiO_2$ aggregates were produced by $TiCl_4$ or titanium isopropoxide oxidation followed by coagulation and sintering.[14] This was observed also with flame-made ZnO nanocrystalline aggregates exhibiting a blueshift of their absorption spectrum with decreasing ZnO crystallite size from about 8 to 1.5 nm.[15] A narrow crystal size distribution is required for this quantum-size effect.

To design reactors for synthesis of nanoparticles exhibiting optimal performance, a better understanding of the parameters affecting PP polydispersity during sintering is required. Here, the sintering of fractal-like particles made by cluster–cluster agglomeration is simulated focusing on the dynamics of their inter-PP distance, $dx/dt$, and PP radius, $dr_p/dt$. So particle restructuring during sintering of fractal-like agglomerates (physically-bonded PPs) to aggregates (chemically- or sinter-bonded PPs) and eventually to compact particles (e.g., spheres) is elucidated through energy and mass balances.[16] The effect of initial PPSD and type or mechanism of sintering on aggregate morphology, PP polydispersity, and surface area mean diameter are investigated.

## Theory

Geometric models frequently describe sintering of agglomerates of PPs by viscous flow,[16,17] grain boundary,[18] and lattice diffusion. Such agglomerates are generated here by

diffusion-limited cluster–cluster agglomeration.[19] Their initial PPSDs have log-normal geometric standard deviation, $\sigma_g = 1.0$ (monodisperse), 1.45, or 2.0. These agglomerates become aggregates upon the onset of sintering and are characterized by their average projected area, $a_a$, PP diameter, $d_{va} = 6v/a$, and number, $n_{va} = 6v/\pi d_{va}^3$, where $v$ is the total volume and $a$ the total surface area of the parent fractal-like particle (agglomerate or aggregate). The $a_a$ influences mass and momentum transfer[20] and, thus, the fractal-like particle mobility diameter, $d_m$, in the free molecular[21] and transition[22] regimes

$$d_m = 2\sqrt{a_a/\pi} \tag{1}$$

A power law between $a_a$ and number of PPs, $n_p$ or $n_{va}$, in an agglomerate or aggregate is[23]

$$n_p = k_a\left(\frac{a_a}{a_p}\right)^{D_\alpha}; \qquad n_{va} = k_a\left(\frac{a_a}{a_{va}}\right)^{D_\alpha} \tag{2}$$

where $a_p$ and $a_{va}$ are the projected areas of monodisperse and polydisperse,[24] respectively, PPs within such fractal-like particles and $k_a$ a constant and $D_\alpha$ a projected area exponent. Combining Eqs. 1 and 2 gives

$$d_m = d_p\left(\frac{n_{va}}{k_a}\right)^{1/(2D_\alpha)} \tag{3}$$

The morphology of fractal-like particles is characterized with the fractal dimension, $D_f$[25]

$$n_p = k_n\left(\frac{r_g}{r_p}\right)^{D_f} \tag{4}$$

where $k_n$ is a constant prefactor and $r_g$ the aggregate radius of gyration.[26] Here, $D_f$ is obtained by the sandbox method[25] and arithmetic averaging over 50 agglomerates or aggregates with identical initial $n_{p,0}$ for each time step. According to this method,[25] a box (sphere) of radius $R_s$ is placed around the PP, which is closest to the center of mass of the agglomerate/aggregate and the mass inside the box is calculated, $m(R_s)$. This box is successively increased in small steps until all PPs are within the box. The slope of $m(R_s)$ vs. $R_s$ in a log–log plot corresponds to $D_f$.

### *Particle sintering*

Sintering is simulated by gradually overlapping PPs in the form or shape of truncated spheres.[16] The approach of PP centers and rate of PP growth are given by mass[27] and energy balances.[28] The overlapping volume is only counted once and the PP radii increase to conserve the mass of the truncated spheres (Eq. 7 in Eggersdorfer et al.[16])

$$\frac{dr_{p,i}}{dt} = -\frac{a_n}{a_i}\frac{dx_i}{dt} \tag{5}$$

where $a_n$ is the cross-sectional neck area, $a_i$ the free PP surface area, and $dx_i/dt$ the change in distance between PP center and neck area (Appendix Figure A1). For viscous flow sintering, $dx_i/dt$ is based on the Frenkel–Eshelby model,[29] which equates the energy gained by surface reduction to the energy dissipated by uniaxial extensional flow, for example, for two equally sized particles[16]

$$\frac{dx_i}{dt^*} = -\frac{2r_{p,0}r_{p,i}x_i}{(2r_{p,i}+2x_i)(2x_i-4r_{p,i})} \tag{6}$$

where $t^* = t/\tau_0$ is the time normalized by the characteristic sintering time $\tau_0$. The approach of particle centers for lattice diffusion is (Appendix)

$$\frac{dx_i}{dt*} = -\frac{r_{p,0}^3}{R\pi}\left(\frac{1}{R_{out}} - \frac{1}{R}\right) \tag{7}$$

where $R$ is the neck radius and $R_{out}$ the outer neck radius (Appendix, Figure A1),[30] and for grain boundary diffusion[18]

$$\frac{dx_i}{dt*} = -\frac{r_{p,0}^4}{a_n}\left(\frac{1}{R_{out}} - \frac{1}{R}\right) \tag{8}$$

The $\tau_0$ for each sintering mechanism is

$$\tau_0 = \frac{\eta r_{p,0}}{\gamma} \quad \text{for viscous flow sintering}[28] \tag{9a}$$

$$\tau_0 = \frac{k_B T r_{p,0}^3}{\pi D_v C_{v0}\gamma\Omega} \quad \text{for lattice diffusion sintering (Appendix)} \tag{9b}$$

$$\tau_0 = \frac{k_B T r_{p,0}^4}{2\pi D_v C_{v0}\delta_{gb}\gamma\Omega} \quad \text{for grain boundary diffusion sintering}[18] \tag{9c}$$

where $\gamma$ is the surface energy, $\eta$ the particle viscosity, $D_v$ the vacancy diffusion coefficient, $\Omega$ the atom or vacancy volume (assumed identical), $k_B$ the Boltzmann constant, $T$ the temperature, $\delta_{gb}$ the grain boundary thickness, and $C_{v0}$ is the equilibrium vacancy concentration beneath a flat surface.[18]

Aggregate restructuring during sintering is simulated using the SHAKE algorithm[31] to fulfill the distance constraints between neighboring PPs, regardless of their number of contacts.[16,18] The particle centers approach each other according to $dx_i/dt^*$ (Eqs. 6–8). So, at each time step, the new particle positions are calculated to constrain pairs of particles to be at a specified distance using Lagrangian multipliers.[32] The free surface, volume, and nonspherical contact areas of the PPs (truncated spheres) are calculated with the Vorlume software.[33] It decomposes the volume of the union of spheres into convex regions using a weighted Delaunay triangulation.[34] Although the PP radius increases and surface area decreases during sintering, its volume remains constant as the multiple overlaps are considered by the triangulation. This increases the geometric PP radius, $r_{p,i}$, as well as $d_{va}$. The volume of a PP is only increased by that of a neighboring PP when these two PPs are completely coalesced: the distance between the PP centers is less than 0.5% of the smaller PP's radius (corresponding to 99.6% volume of the fully fused sphere). Then, the smaller particle is deleted and the number of PPs ($n_p$) is reduced by one until only one spherical particle is left at the end of sintering, $n_p = n_{va} = 1$.

Analytical solutions for the initial stage sintering of two equally sized spherical particles are[35]

$$\left(\frac{R}{r_{p,0}}\right)^y = \frac{B}{(r_{p,0})^w}t \tag{10a}$$

$$\left(\frac{\Delta x}{x_0}\right)^{y/2} = -\frac{B}{2^y(r_{p,0})^w}t \tag{10b}$$

where $r_{p,0}$ is the initial PP radius, and $B$, $y$, and $w$ are parameters depending on mechanism[35]

$$B = 3\gamma/2\eta,\ w = 1,\ \text{and}\ y = 2 \quad \text{for viscous flow}^{28} \tag{10c}$$

$$B = 80\pi D_v \gamma \Omega / k_B T,\ w = 3,\ \text{and}\ y = 5 \quad \text{for lattice diffusion}^{36} \tag{10d}$$

$$B = 96 D_v \delta_{gb} \gamma \Omega / k_B T,\ w = 4,\ \text{and}\ y = 6 \ \text{for grain boundary diffusion}^{30} \tag{10e}$$

Viscous flow sintering is dominant for amorphous materials (e.g., polymers[37] and silica[36]), whereas lattice and grain boundary diffusion are possible for crystalline materials (e.g., $TiO_2$[38] and ZnO[39]), although surface diffusion becomes dominant for lower temperatures,[40] smaller particles,[36] and aerosol nanoparticles with their free (unconstrained) surfaces.[41] The particle-size dependence on sintering mechanism strongly affects the sintering rate or time. Therefore, it is crucial to account for particle polydispersity during sintering.[42]

## Results and Discussion

### *Validation and morphology evolution of aggregates with polydisperse PPs*

The neck growth and approach of particle centers of two equally sized particles are calculated with Eqs. 6–8 and conservation of mass (Eq. 5) and compared to analytical solutions at the onset of sintering (Eqs. 10) while multiparticle sintering simulations have been validated already.[16]

Sintering by viscous flow,[16] grain boundary,[18] and lattice diffusion of cluster–cluster made agglomerates[19] consisting initially of 16, 64, 256, and 512 PPs with initial $\sigma_{g,0} = 1.0$, 1.45, and 2.0 was simulated here. Averages are taken over 50 agglomerates for each size and sintering mechanism. Figure 1 shows exemplary snapshots of a single agglomerate consisting initially of 256 PPs and $D_{f,0} = 1.79 \pm 0.07$ with $\sigma_{g,0} = 1.45$ undergoing sintering by the above mechanisms at dimensionless time, $\Theta = (t/\tau_0)^{2/y} = 0$, 1, 3, 6, 10, and 60. For example, $\Theta = 1$ corresponds to $t = \tau_0 = 13.8$ s for a $SiO_2$ particle with $r_{p,0} = 5$ nm that sinters by viscous flow at $T = 1500$ K while for $TiO_2$ that sinters by grain boundary diffusion $\Theta = 1$ corresponds to $t = \tau_0 = 0.013$ s. At $T = 1700$ K and same $r_p$, $\Theta = 1$ corresponds to $t = \tau_0 = 0.0132$ and $5.4 \times 10^{-4}$ s for $SiO_2$ and $TiO_2$, respectively.[43]

The color represents the curvature (= 1/radius) of the particle surface (blue = small radius and red = large radius) within the aggregate. The broader the PPSD, the more colorful are the aggregates. At the onset of sintering ($\Theta > 0$), necks form between PPs in contact converting the agglomerate to aggregate. At $\Theta = 1$, the aggregate keeps its chain-like morphology, but its structure has changed from the initial $D_f = 1.79$ to $D_f \approx 1.72$, 1.69, and 1.61 for viscous flow (a), lattice diffusion (b), and grain boundary diffusion sintering (c), respectively. Then, individual chains or branches of such aggregates straighten out[16] decreasing its $D_f$ as has been seen experimentally.[44] After that ($\Theta = 3$–10), branches shrink and the aggregate surface becomes smoother as the necks grow larger and its $D_f$ increases.

At junctions where two branches meet, a sharp concave edge remains (e.g., $\varphi$ in Figure 1a at $\Theta = 3$–10). The concave structure between two branches fills rather fast as has been seen by molecular dynamics simulation of $TiO_2$ sintering.[41] As a result, such branches gradually fuse forming more compact particles (e.g., at $\Theta = 10$). Sintering by grain boundary diffusion results in slightly more compact shapes ($D_f \approx 2.6$) than lattice diffusion or viscous flow ($D_f \approx 2.2$) at $\Theta = 10$.

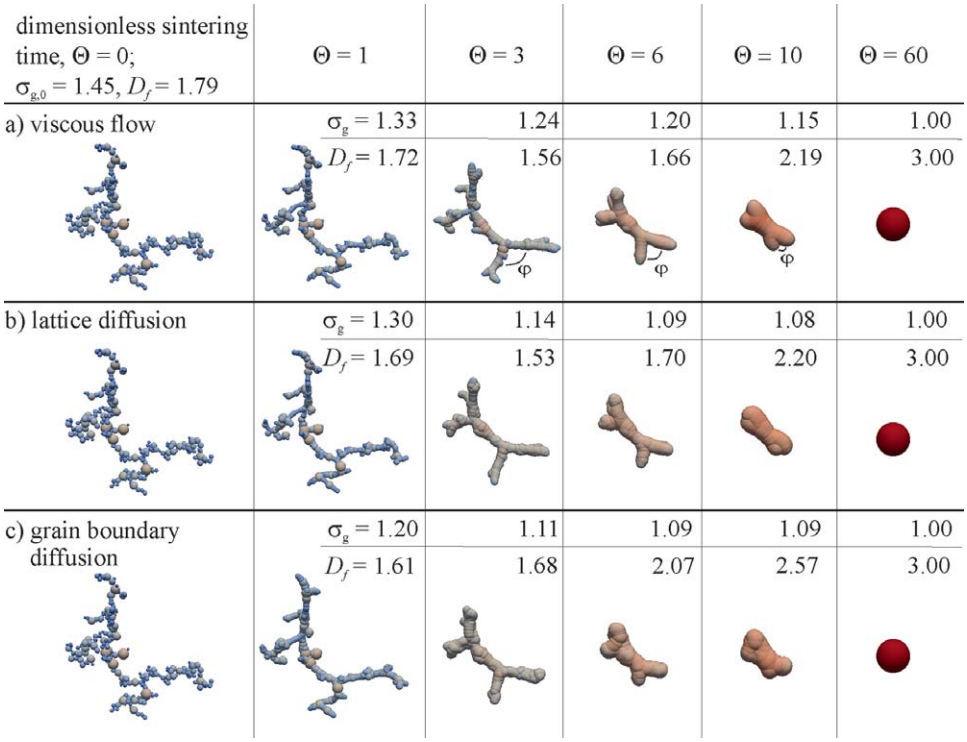


**Figure 1. Snapshots of an aggregate of initially $n_{p,0} = 256$ PPs that sinter by viscous flow (a), lattice (b), and grain boundary diffusion (c).**

**The shown geometric standard deviation $\sigma_g$ is calculated with the diameters of consitituent PPs. The color of each particle changes with its curvature (= 1/radius: blue = high curvature and red = low curvature). [Color figure can be viewed in the online issue, which is available at wileyonlinelibrary.com.]**

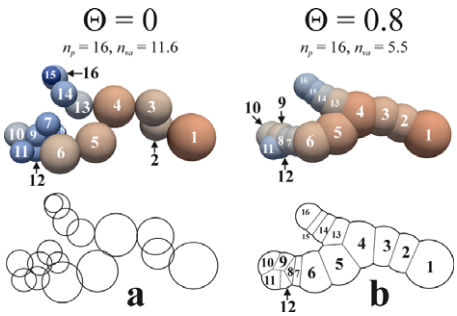


**Figure 2. The transformation of an initial agglomerate (a) of 16 PPs to an aggregate (b) after sintering by grain boundary diffusion for dimensionless time Θ = 0.8.**

**The sinter neck or grain boundaries between neighboring particles are sketched with thin lines. The diameter of constituent PPs (depicted as truncated spheres in the aggregate) represents the maximum extension of PP or crystal size. The number of PPs, $n_p$, remains constant while the average PP number, $n_{va}$, decreases during sintering due to the decreasing surface area of the parent aggregate. [Color figure can be viewed in the online issue, which is available at wileyonlinelibrary.com.]**

Throughout sintering or coalescence (Θ = 1–10), however, only small differences in aggregate morphology are apparent among the three sintering mechanisms. This indicates that these mechanisms lead to quite a similar restructuring pathway, although there are strong differences in actual time and size stemming from their differing sintering parameters (Eqs. 9 and 10).

### *Detailed restructuring and PPSD of aggregates*

The detailed PPSD is monitored during sintering by tracing numerically the center and radius of each PP in the starting agglomerate or aggregate. Figure 2a shows an agglomerate of $n_p = 16$ PPs ($n_{va} = 11.6$) having an initial (Θ = 0) size distribution of $\sigma_{g,0} = 1.45$ and below its cross section. At Θ = 0.8 and sintering by grain boundary diffusion, the initial agglomerate has become an aggregate with a narrower size distribution of PPs ($\sigma_g \approx 1.25$), and $n_{va} = 5.5$ as its free surface area has decreased. The PPSD changes as the geometric radius of the spherical PPs (truncated spheres) increases with approaching particle centers to compensate for the overlapping volume and conserve the PP mass. So, the overlapping volume is redistributed among the remaining PPs (Eq. 5). Besides the sintering mechanism, the PP growth rate depends also on geometry: number of particle contacts, size of the neighboring PPs, and size itself.

At the onset of sintering, PPs start to fuse or coalesce and both $d_{va}$ and $d_p$ grow according to Eq. 5. Grain boundaries or sinter necks between particles are marked by a thin line at the bottom of Figure 2b. For example, a comparison of PP #15 in Figure 2 at Θ = 0 (a) and 0.8 (b) shows a significant broadening in curvature or equivalent PP diameter (and change in color) similar to the other small PPs #7–10. At the same time, isolated PPs hardly grow (e.g., PP #1 and 16) in contrast to others. For example, PP #5 develops a third neck with PP #13 (besides #4 and 6) and grows noticeably despite its initial large size. Aggregate branches straighten (e.g., PPs #1–4 in Figure 2b), similar to molecular dynamics of silicon sintering (Figure A1 in Hawa and Zachariah[45]). Individual PP sizes are related to the maximum extension of crystalline areas in polycrystalline particles forming the so-called twin-crystal structures.

Figure 3 shows the evolution (Θ = 0–10) of PPSD during sintering by grain boundary diffusion having initially (Θ = 0, circles), $d_{p,g} = 20$ nm, $n_{p,0} = 256$, and $\sigma_{g,0} = 1.45$ (Figure 1c). The $d_{p,i}$ of all PPs in 50 different agglomerates is used to calculate $\sigma_g$ and $d_{p,g}$. At Θ = 1 (triangles), the small tail of the PPSD narrows rapidly to result in $\sigma_g \approx 1.20$ (Figure 1c). For sintering by grain boundary diffusion with a strong size dependence ($w = 4$, Eq. 10e), smaller particles sinter much faster than larger ones affecting initially the small tail. This is consistent with two-dimensional (2-D) sectional simulations of sintering of $TiO_2$ aggregates with polydisperse PPSD (Figure 5 in Heine and Pratsinis[14]), however, without having here the restriction of two particle sintering.[28]

Sintering between unequally sized PPs is dominated by the smallest.[46,47] In Figure 3, the large tail hardly changes up to Θ = 1, and the mean PP diameter is only affected by sintering of small PPs and sinter-neck formation. So at Θ = 1, the aggregate shape ($D_f \approx 1.61$, Figure 1c) is similar to the initial (Θ = 0) agglomerate structure ($D_f \approx 1.79$, Figure 1c). When PPs reach a similar size and hence a narrow size distribution (here at about Θ = 3, diamonds), their structure ($D_f = 1.68$) is more open (less compact) than the initial one due to branch straightening.[16] Later on (Θ = 3–10) as rapid filling of the concave regions between branches takes place[41] and the $\sigma_g$ of PP is rather constant ($\sigma_g \approx 1.1$), aggregates start to discernibly become more compact ($D_f \approx 2.07$ at Θ = 6). The individual branches shrink, decreasing in length but increasing in diameter (Figure 1c).

From Θ = 1 to 10, the aggregate shape changes significantly: from an open-structured and chain-like ($D_f = 1.61$ at Θ = 1) to a compact particle ($D_f \approx 2.57$ at Θ = 10) with a nearly smooth surface (Figure 1). Sharp edges with small outer neck radii exclusively remain at the junction of two or more

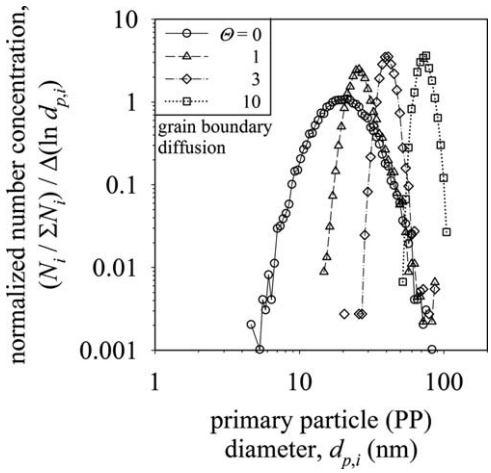


**Figure 3. The PPSD of aggregates consisting initially of 256 PPs and that sinter by grain boundary diffusion at dimensionless times $\Theta = (t/\tau_0)^{2/y}$ = 0 (circles), 1 (triangles), 3 (diamonds), and 10 (squares).**

**Initially the PPs have $\sigma_{g,0} = 1.45$ of the self-preserving size distribution by Brownian coagulation. Small particles sinter faster than larger ones so the small tail of the distribution narrows at the beginning of sintering Θ = 0–1. Later also the large particles sinter resulting in a narrow size distribution with $\sigma_g \approx 1.1$ and $d_{p,g} = 73$ nm at Θ = 10 (squares).**

former branches. During this restructuring, all PPs grow shifting the PP distribution to larger sizes with $d_{p,g} = 73$ nm. Then, PPs have a narrow size distribution and heavily overlap, so original PPs are no longer distinguished as individual entities. This is an indication for a compact particle, with a rather rough surface as complete coalescence to a perfect sphere takes much, much longer ($\Theta = 60$, Figure 1).

### *Effect of sintering mechanism on PP growth and size distribution*

Figure 4 quantifies the progress of aggregate restructuring of Figure 1 (and 3) by showing the evolution of (a) $\sigma_g$ and (b) $d_{va}$ as a function of dimensionless time $\Theta$ during sintering by viscous flow (solid line), lattice (broken line), and grain boundary diffusion (gbd, dotted line) of initial agglomerates with $n_{p,0} = 256$ and $\sigma_{g,0} = 1.45$. Grain boundary diffusion reduces $\sigma_g$ most rapidly (with $\Theta$), as it has the strongest size dependence ($w = 4$ in Eqs. 10). The initial reduction in $\sigma_g$ is driven by sintering of the small particles in an aggregate (Figure 3) and by neck formation at their contacts (Figure 2). Smaller particles sinter faster than larger ones leading to a rapid reduction of $\sigma_g$ to ~1.1 at $\Theta \approx 4$ for lattice and grain boundary diffusion. There is competition between two effects: accelerated growth with increasing number of particle contacts vs. reduced growth with increasing particle size. When a particle grows larger than its neighbors, because it has more contacts, its growth slows down immediately by the strong size dependence of sintering. As a result, neighboring particles catch up, narrowing the size distribution ($\sigma_g \approx 1.1$). The aggregate becomes more compact and slowly approaches a sphere.

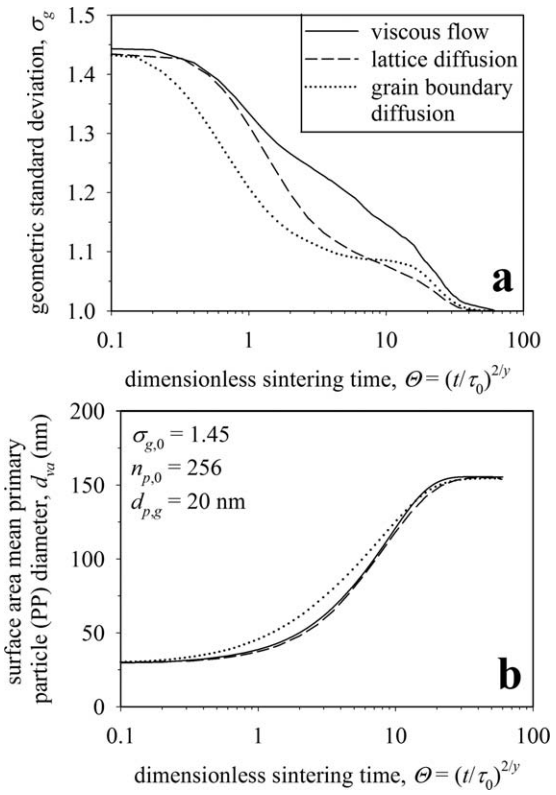


**Figure 4. The evolution of PP (a) geometric standard deviation and (b) surface area mean diameter, agglomerates that sinter by viscous flow, lattice and grain boundary diffusion (Figure 1).**

**The broadest PPSD is obtained by viscous flow, which has the weakest size dependence on the neck growth rate ($w = 1$, Eqs. 10). In grain boundary diffusion, differences in particle radii are balanced most effectively ($w = 4$, Eqs. 10) resulting in the narrowest distribution. The evolution of PP $d_{va}$ is nearly independent of sintering mechanism in contrast to that of the PPSD that shows significant variation among the three mechanisms.**

The evolution of PPSD by sintering through lattice diffusion lies between viscous flow and gbd except at the end of sintering for $\Theta > 10$, consistent with its weaker dependence of sintering on particle size ($w = 3$ in Eq. 10). Viscous sintering shows the slowest narrowing of PPSD, as it has the weakest size dependence ($w = 1$). The narrower size distribution of gbd is again an indication for a rough particle surface. Both lattice diffusion and viscous flow sintering result in compact particles at $\Theta = 10$ with slightly smoother surface (Figure 1) than gbd.

As shown in Figure 1, the evolutions of aggregate structure are quite similar regardless of sintering mechanism. So these three mechanisms lead to a fully coalesced sphere nearly at the same dimensionless time (Figure 4b, $\Theta \approx 30$). In terms of $\Theta$, sintering by gbd (dotted line) is slightly faster than that by viscous flow and lattice diffusion. Note again that $\tau_0$ depends on several particle properties (Eqs. 9), so the absolute time $t$ for each mechanism is different. Nevertheless, the $\Theta$ of monodisperse two-particle sintering (Eqs. 9) reduces to nearly a single line (Figure 4b) the evolution of $d_{va}$ for aggregates of polydisperse particles by the three sintering mechanisms.

### *Effect of initial PPSD shape and PP number on PP growth and size distribution*

Figure 5 shows the evolution of (a) $\sigma_g$ and (b) $d_{va}$ by grain boundary diffusion sintering for agglomerates consisting of PPs with $\sigma_{g,0} = 1.0$ (broken line), 1.45 (dotted line), and 2.0 (solid line). In Figure 5b, the initial $d_{va,0}$ increases for increasing $\sigma_{g,0}$ to assure the same $d_{p,g}$ and $n_{p,0}$ for all agglomerates. Both average agglomerate surface area and mass increase with increasing $\sigma_{g,0}$ resulting in a larger initial $d_{va}$ and, thus, taking longer to fully coalesce. The initially monodisperse PPs (broken line) grow slightly polydisperse with a maximum $\sigma_g \approx 1.1$ at $\Theta \approx 10$ (Figure 5a). There the aggregate is a slightly elongated or oval particle with a homogeneous "diameter" (Figure 2 in Eggersdorfer et al.[18]). The PP growth rate ($dr_p/dt$) depends on the number of contacts, so particles at the end or junctions of branches experience a slower or faster growth, respectively, which affects naturally the sintering rate of the entire aggregate. Still their size distribution stays narrow throughout sintering (for all investigated $n_{p,0} = 16$–$512$). Agglomerates with PP $\sigma_{g,0} = 1.45$ attain also $\sigma_g \approx 1.1$ at $\Theta \approx 10$. However, agglomerates with increasing $\sigma_{g,0}$ need longer time to fully coalesce ($\sigma_g = 1$), as they have a larger initial $d_{va}$ (Figure 5b).

Figure 6 shows the effect of initial PP number $n_{p,0}$ in agglomerates with $\sigma_{g,0} = 1.45$ on the evolution of (a) $\sigma_g$ and (b) $d_{va}$ during sintering by grain boundary diffusion. Agglomerates with more PPs have a larger surface area, mass, and spatial expansion, so they need more time to fully coalesce ($dd_{va}/d\Theta = 0$, Figure 6b). Neck formation between neighbors at the beginning of sintering ($\Theta < 1$) is independent of initial agglomerate size and so the initial reduction in $\sigma_g$ is identical for all $n_{p,0}$ (Figure 6a). Aggregates of few nanoparticles (e.g., $n_{p,0} = 16$) consist of mainly one branch and have already attained an oval shape at $\sigma_g \approx 1.1$. So they

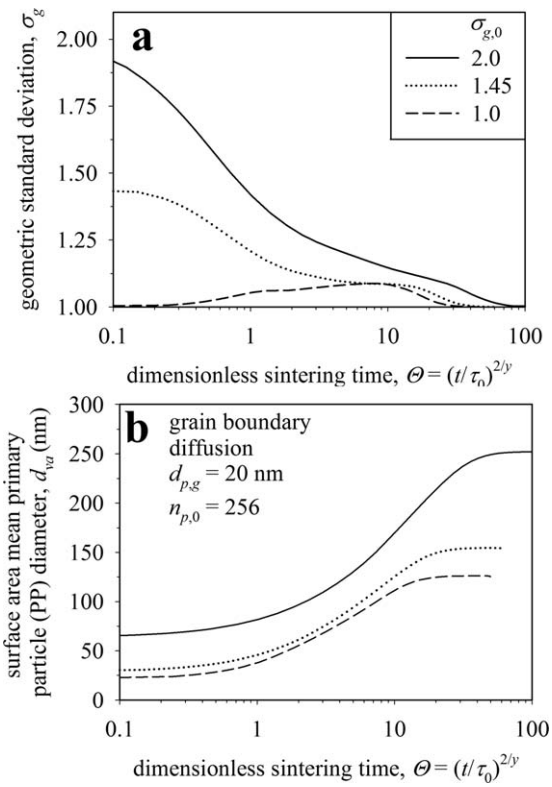


**Figure 5. The effect of initial PPSD shape on the evolution of PP (a) geometric standard deviation $\sigma_g$ and (b) surface area mean diameter $d_{va}$ for agglomerates that sinter by grain boundary diffusion (Figure 1).**

**Agglomerates with the same geometric mean diameter $d_{p,g}$ but larger $\sigma_{g,0}$ have a larger surface area and mass and take longer to fully coalesce. The PP distribution with $\sigma_{g,0} = 1$ (broken line, monodisperse) remains narrow during sintering with a maximum $\sigma_g \approx 1.1$. Aggregates with $\sigma_{g,0} = 1.45$ (dotted line) reach also $\sigma_g \approx 1.1$ after $\Theta = 10$, however, require more time to fully coalesce as their $d_{va}$ is larger (b). Aggregates with $\sigma_{g,0} = 2.0$ experience a rapid decrease of $\sigma_g$ at the beginning of sintering $\Theta < 2$ which slows down at the end of sintering for $\sigma_g < 1.3$.**

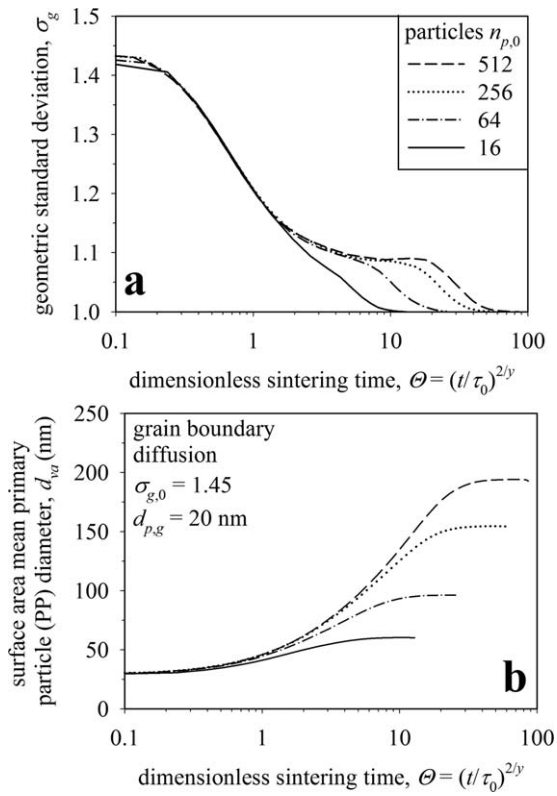


**Figure 6. The effect of initial number of PPs per agglomerate, $n_{p,0}$, on the evolution of PP (a) $\sigma_g$ and (b) $d_{va}$ for agglomerates that sinter by grain boundary diffusion.**

**At the beginning of sintering ($\Theta < 1$) both $\sigma_g$ and $d_{va}$ are independent of $n_{p,0}$ as necks between neighboring particles form independent of the total aggregate size. Later, PP growth and $\sigma_g$ depend on $n_{p,0}$ as larger agglomerates have a bigger spatial extension, larger surface area and mass, requiring more time to coalesce. Nevertheless, the rapid initial reduction in polydispersity resulting in a low $\sigma_g \approx 1.1$ is maintained during sintering for larger $n_{p,0}$.**

continue to coalesce to a sphere. In contrast, larger aggregates ($n_{p,0} > 16$) of several branches still have an elongated shape by the time the PPSD reaches $\sigma_g \approx 1.1$ (Figure 1, $\Theta = 3$–10). These elongated structures lead to an oval particle keeping, however, that narrow distribution independent of initial size, $n_{p,0}$. So aggregates sintered by gbd attain rapidly a narrow PPSD, as observed in flame synthesis of ZnO that exhibits a quantum dot behavior that is characteristic of particles having a narrow size distribution.[15]

### *Scaling of projected aggregate area during sintering*

Figure 7 shows the power law scaling of Eq. 2 for aggregate sintering by viscous flow (triangles), lattice (squares),

**Table 1. Projected Area Exponent $D_\alpha$ and Prefactor $k_a$ for Different Initial PPSDs ($\sigma_{g,0}$) and Sintering Mechanisms**

| $\sigma_{g,0}$ | Sintering Mechanism | $D_\alpha$ | $\bar{D}_\alpha$ | $k_a$ | $\bar{k}_a$ |
|---|---|---|---|---|---|
| 1.0 | Viscous | 1.07 ± 0.002 | | 1.00 ± 0.003 | |
| | Lattice diffusion | 1.07 ± 0.002 | 1.07 ± 0.002 | 0.99 ± 0.003 | 1.00 ± 0.003 |
| | Grain boundary diffusion | 1.07 ± 0.002 | | 0.99 ± 0.003 | |
| 1.45 | Viscous | 1.07 ± 0.002 | | 1.00 ± 0.003 | |
| | Lattice diffusion | 1.08 ± 0.002 | 1.08 ± 0.002 | 1.00 ± 0.003 | 1.00 ± 0.003 |
| | Grain boundary diffusion | 1.08 ± 0.002 | | 0.99 ± 0.003 | |
| 2.0 | Viscous | 1.10 ± 0.003 | | 0.99 ± 0.004 | |
| | Lattice diffusion | 1.12 ± 0.002 | 1.11 ± 0.002 | 0.97 ± 0.004 | 0.97 ± 0.004 |
| | Grain boundary diffusion | 1.12 ± 0.002 | | 0.97 ± 0.004 | |
| 1.0–2.0 | All | 1.082 ± 0.001 | | 0.990 ± 0.001 | |

The $D_\alpha$ and $k_a$ are practically independent of sintering mechanism.

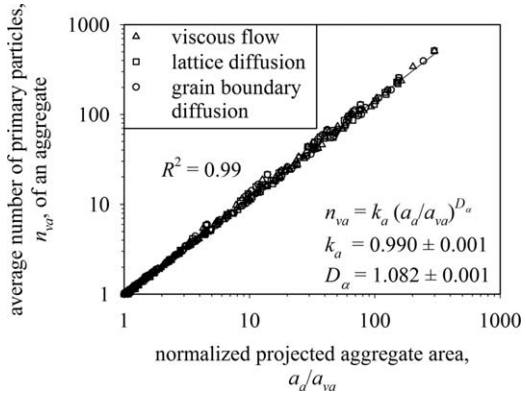


**Figure 7. The average number of PPs in aggregate as a function of its normalized projected area during sintering or coalescence of the aggregate by viscous flow (triangles), lattice (squares) and grain boundary diffusion sintering (circles) for initial PP $\sigma_{g,0}$ = 1–2.**

**There is nearly no effect of sintering mechanism and PP polydispersity on the power law of Eq. 2, although the neck growth rate and sintering time differs significantly (exponents w and y in Eqs. 10). The $D_\alpha = 1.082$ and $k_a = 0.99$ are in agreement with experimental measurements.[48]**

and grain boundary diffusion (circles). This relation is useful in mass-mobility characterization of agglomerates and aggregates with PPs in the free molecular and transition regime to determine the $d_{va}$ and specific surface area (SSA) in almost real-time (Eq. 8 in Eggersdorfer et al.[18]). Most notably, it is independent of sintering mechanism resulting in $k_a = 0.990 \pm 0.001$ and $D_\alpha = 1.082 \pm 0.001$ with $R^2 = 0.99$ for $\sigma_{g,0} = 1$–2 (Table 1). So $n_{va}$ and the aggregate SSA can be determined from $a_a$,[18] regardless of material, sinter mechanism or PP polydispersity, as $k_a$ and $D_\alpha$ remain constant during sintering. Equation 3 with the above $k_a$ and $D_\alpha$ for $\sigma_{g,0} = 1$–2 gives: $d_m = d_p(n_{va})^{0.46}$, in agreement with simulations and experiments of the mobility of cluster–cluster agglomerates (Eq. 24 in Sorensen[48]).

The effect of $\sigma_{g,0}$ on projected area exponent $D_\alpha$ and prefactor $k_a$ is summarized in Table 1 for the three sintering mechanisms studied here. A broader initial PPSD results in a larger $D_\alpha$ while $k_a$ is almost constant around one. Eggersdorfer and Pratsinis[49] showed that $D_\alpha$ decreases with increasing PP polydispersity. Once agglomerates start sintering, the polydispersity is reduced and $D_\alpha$ is even larger than that for initially monodisperse particles. This is a consequence of using $d_{va}$ as average diameter for polydisperse aggregates. The large tail of the distribution is weighed stronger ($d^2$-dependence) and, thus, both $n_{va}$ and $a_a/a_{va}$ are lower compared to monodisperse agglomerates. The slope ($D_\alpha$ increases as the aggregates coalesce to a compact sphere with $n_{va} = a_a/a_{va} = 1$.

## Conclusions

Aggregate sintering by viscous flow, lattice, and grain boundary diffusion is simulated by multiparticle dynamics focusing on PP growth and surface area evolution. Small PPs sinter faster than larger ones and, thus, vanish rapidly narrowing the PPSD. The size and dynamic exponents of sintering rates for the neck growth rate depend, however, on sintering mechanisms resulting in slightly different PPSDs during sintering. Nevertheless, this hardly affects the evolution of average PP diameter and aggregate surface area normalized by the characteristic time of sintering. A power law (Eq. 2 with $k_a = 0.990$ and $D_\alpha = 1.082$) holds between aggregate projected area and average number of PPs. This is in agreement with experiments (Eq. 24 in Sorensen[48]), independent of sintering mechanism and initial PPSD. This is important for aggregate characterization by mass-mobility measurements and in design of aerosol reactors for nanoparticle manufacturing by coagulation and sintering.

## Acknowledgments

Financial support by ETH Research Grant (ETHIIRA) ETH-11 09-1 and the Europen Research Council under the European Union's Seventh Framework Programme (FP7/2007-2013)/ERC grant agreement n° 247283 as well as discussions with Dr. Dirk Kadau (currently at Wärtsilä Switzerland Ltd., Winterthur) are gratefully acknowledged. This article (Y3.03) received a Best Poster Award at the 2012 Fall Meeting of the Materials Research Society, Boston, MA, USA, November 25–30, http://www.ptl.ethz.ch/box_feeder/Max_List.JPG.

## Notation

$a$ = surface area, $m^2$
$B$ = auxiliary variable for Eqs. 10
$C_v$ = fraction of sites occupied by vacancies
$D_\alpha$ = projected area exponent, Eq. 2
$D_f$ = effective fractal dimension, Eq. 4
$D_v$ = vacancy diffusion coefficient, $m^2\ s^{-1}$
$d$ = diameter, m
gbd = grain boundary diffusion
$J$ = flux of atoms, $\#\ s^{-1}\ m^{-5}$
$k_B$ = Boltzmann constant, $m^2\ kg\ s^{-2}\ K^{-1}$
$k_a$ = prefactor for Eq. 2
$k_n$ = prefactor for Eq. 4
$m$ = mass, kg
$N_A$ = Avogadro number, $mol^{-1}$
$n$ = number
PP = primary particle
$Q$ = activation energy, $kg\ m^2\ s^{-2}\ mol^{-1}$
$R$ = neck radius, m
$R_s$ = sandbox radius, m
$r$ = radius, m
$r_g$ = radius of gyration, m
$T$ = temperature, K
$t$ = time, s
$t^*$ = dimensionless time
$v$ = volume, $m^3$
$w$ = scaling Eqs. 10
$x$ = particle center to neck distance, m
$y$ = scaling Eqs. 10

### *Greek letters*

$\gamma$ = surface energy, $kg\ s^{-2}$
$\delta_{gb}$ = grain boundary thickness, m
$\eta$ = viscosity, $kg\ s^{-1}\ m^{-1}$
$\Theta$ = dimensionless time
$\sigma_g$ = geometric standard deviation
$\tau$ = characteristic sintering time, s
$\varphi$ = angle between aggregate branches
$\Omega$ = volume of atom or vacancy, $m^3$

### *Subscripts*

0 = initial
a = average projected
g = geometric
l = lattice

m = mobility
n = neck
out = outer
p = primary particle
va = surface area mean, based on $d_{va}$

## Literature Cited


1. Kingery WD, Bowen JK, Uhlmann DR. Introduction to Ceramics. New York: Wiley, 1976.
2. Reed MA, Randall JN, Aggarwal RJ, Matyi RJ, Moore TM, Wetsel AE. Observation of discrete electronic states in a zero-dimensional semiconductor nanostructure. *Phys Rev Lett*. 1988;60(6):535–537.
3. Kreibig U, Vollmer M. Optical Properties of Metal Clusters. Berlin: Springer, 1995.
4. Teleki A, Suter M, Kidambi PR, Ergeneman O, Krumeich F, Nelson BJ, Pratsinis SE. Hermetically coated superparamagnetic $Fe_2O_3$ particles with $SiO_2$ nanofilms. *Chem Mater*. 2009;21(10):2094–2100.
5. Huynh WU, Dittmer JJ, Alivisatos AP. Hybrid nanorod-polymer solar cells. *Science*. 2002;295(5564):2425–2427.
6. Sotiriou GA, Sannomiya T, Teleki A, Krumeich F, Voeroes J, Pratsinis SE. Non-toxic dry-coated nanosilver for plasmonic biosensors. *Adv Funct Mater*. 2010;20(24):4250–4257.
7. Colvin VL, Schlamp MC, Alivisatos AP. Light-emitting-diodes made from cadmium selenide nanocrystals and a semiconducting polymer. *Nature*. 1994;370(6488):354–357.
8. Pratsinis SE. Flame aerosol synthesis of ceramic powders. *Prog Energy Combust Sci*. 1998;24(3):197–219.
9. Friedlander SK, Wang CS. Self-preserving particle size distribution for coagulation by Brownian motion. *J Colloid Interface Sci*. 1966;22(2):126–132.
10. Landgrebe JD, Pratsinis SE. Gas-phase manufacture of particulates—interplay of chemical-reaction and aerosol coagulation in the free-molecular regime. *Ind Eng Chem Res*. 1989;28(10):1474–1481.
11. Bensberg A, Roth P, Brink R, Lange H. Modeling of particle evolution in aerosol reactors with coflowing gaseous reactants. *AIChE J*. 1999;45(10):2097–2107.
12. Seinfeld JH, Pandis SN. Atmospheric Chemistry and Physics: From Air Pollution to Climate Change, 2nd ed. Hoboken, NJ: Wiley, 2006.
13. Tsantilis S, Pratsinis SE. Evolution of primary and aggregate particle-size distributions by coagulation and sintering. *AIChE J*. 2000;46(2):407–415.
14. Heine MC, Pratsinis SE. Polydispersity of primary particles in agglomerates made by coagulation and sintering. *J Aerosol Sci*. 2007;38(1):17–38.
15. Madler L, Stark WJ, Pratsinis SE. Rapid synthesis of stable ZnO quantum dots. *J Appl Phys*. 2002;92(11):6537–6540.
16. Eggersdorfer ML, Kadau D, Herrmann HJ, Pratsinis SE. Multiparticle sintering dynamics: from fractal-like aggregates to compact structures. *Langmuir*. 2011;27(10):6358–6367.
17. Pokluda O, Bellehumeur CT, Vlachopoulos J. Modification of Frenkel's model for sintering. *AIChE J*. 1997;43(12):3253–3256.
18. Eggersdorfer ML, Kadau D, Herrmann HJ, Pratsinis SE. Aggregate morphology evolution by sintering: number and diameter of primary particles. *J Aerosol Sci*. 2012;46:7–19.
19. Botet R, Jullien R, Kolb M. Hierarchical model for irreversible kinetic cluster formation. *J Phys A: Math Gen*. 1984;17(2):L75–L79.
20. Filippov AV, Rosner DE. Energy transfer between an aerosol particle and gas at high temperature ratios in the Knudsen transition regime. *Int J Heat Mass Transfer*. 2000;43(1):127–138.
21. Meakin P. Fractal aggregates. *Adv Colloid Interface Sci*. 1988;28(4):249–331.
22. Rogak SN, Flagan RC, Nguyen HV. The mobility and structure of aerosol agglomerates. *Aerosol Sci Technol*. 1993;18(1):25–47.
23. Medalia AI. Morphology of aggregates. 1. Calculation of shape and bulkiness factors—application to computer-simulated random flocs. *J Colloid Interface Sci*. 1967;24(3):393–404.
24. Al Zaitone B, Schmid HJ, Peukert W. Simulation of structure and mobility of aggregates formed by simultaneous coagulation, sintering and surface growth. *J Aerosol Sci*. 2009;40(11):950–964.
25. Forrest SR, Witten TA. Long-range correlations in smoke-particle aggregates. *J Phys A: Math Gen*. 1979;12(5):L109–L117.
26. Jullien R, Botet R. Aggregation and Fractal Aggregates. River Edge, NJ: World Scientific, 1987.
27. Kadushnikov RM, Skorokhod VV, Kamenin IG, Alievskii VM, Nurkanov EY, Alievskii DM. Computer simulation of spherical particle sintering. *Powder Metall Met Ceram*. 2001;40(3–4):154–163.
28. Frenkel J. Viscous flow of crystalline bodies under the action of surface tension. *J Phys (USSR)*. 1945;9:385–391.
29. Eshelby JD. "Discussion" in A.J. Shaler, "Seminar on the Kinetics of Sintering". *Metals Trans*. 1949;185:806–807.
30. Coble RL. Initial sintering of alumina and hematite. *J Am Ceram Soc*. 1958;41(2):55–62.
31. Ryckaert JP, Ciccotti G, Berendsen HJC. Numerical-integration of Cartesian equations of motion of a system with constraints—molecular-dynamics of *n*-alkanes. *J Comput Phys*. 1977;23(3):327–341.
32. Allen MP, Tildesley DJ. Computer Simulation of Liquids. New York: Oxford University Press, 2000.
33. Cazals F, Kanhere H, Loriot S. Computing the volume of a union of balls: a certified algorithm. *ACM T Math Softw*. 2011;38(1):1–20.
34. Liang J, Edelsbrunner H, Fu P, Sudhakar PV, Subramaniam S. Analytical shape computation of macromolecules: I. Molecular area and volume through alpha shape. *Proteins*. 1998;33(1):1–17.
35. Rahaman MN. Sintering of Ceramics. Boca Raton, FL: CRC Press, 2008.
36. Kuczynski GC. Sintering Processes. New York: Plenum Press, 1980.
37. Bellehumeur CT, Bisaria MK, Vlachopoulos J. An experimental study and model assessment of polymer sintering. *Polym Eng Sci*. 1996;36(17):2198–2207.
38. Anderson HU. Initial sintering of rutile. *J Am Ceram Soc*. 1967;50(5):235–238.
39. Ewsuk KG, Ellerby DT, DiAntonio CB. Analysis of nanocrystalline and microcrystalline ZnO sintering using master sintering curves. *J Am Ceram Soc*. 2006;89(6):2003–2009.
40. Chiang YM, Birnie DP, Kingery WD. Physical Ceramics. New York: Wiley, 1997.
41. Buesser B, Grohn AJ, Pratsinis SE. Sintering rate and mechanism of $TiO_2$ nanoparticles by molecular dynamics. *J Phys Chem C*. 2011;115(22):11030–11035.
42. German RM. Sintering Theory and Practice. New York: Wiley, 1996.
43. Grass RN, Tsantilis S, Pratsinis SE. Design of high-temperature, gas-phase synthesis of hard or soft $TiO_2$ agglomerates. *AIChE J*. 2006;52(4):1318–1325.
44. Camenzind A, Schulz H, Teleki A, Beaucage G, Narayanan T, Pratsinis SE. Nanostructure evolution: from aggregated to spherical $SiO_2$ particles made in diffusion flames. *Eur J Inorg Chem*. 2008;2008(6):911–918.
45. Hawa T, Zachariah MR. Development of a phenomenological scaling law for fractal aggregate sintering from molecular dynamics simulation. *J Aerosol Sci*. 2007;38(8):793–806.
46. Yadha V, Helble JJ. Modeling the coalescence of heterogeneous amorphous particles. *J Aerosol Sci*. 2004;35(6):665–681.
47. Westerhoff F, Zinetullin R, Wolf DE. Kinetic monte-carlo simulations of sintering. In: Garcia-Rojo R, Herrmann HJ, McNamara S, editors. Powders and Grains. Rotterdam: Balkema, 2005:641–645.
48. Sorensen CM. The mobility of fractal aggregates: a review. *Aerosol Sci Technol*. 2011;45(7):755–769.
49. Eggersdorfer ML, Pratsinis SE. The structure of agglomerates consisting of polydisperse particles. *Aerosol Sci Technol*. 2012;46(3):347–353.


## Appendix: Lattice Diffusion

A grain boundary forms at the neck of nanoparticles in contact with two misaligned crystals. The high particle curvature in the neck induces a stress gradient resulting in a diffusive flux of atoms $J$ from the neck center (source) to its surface (sink)[40]

$$J = \frac{D_v}{\Omega}\frac{dC_v}{dR} \tag{A1}$$

where $dC_v/dR$ is the vacancy concentration gradient, $R$ the neck radius, $C_v$ the fraction of sites occupied by vacancies and $\Omega$ the volume of an atom or vacancy. During sintering by grain boundary diffusion, the atoms diffuse along the grain boundary (Figure A1).[36]

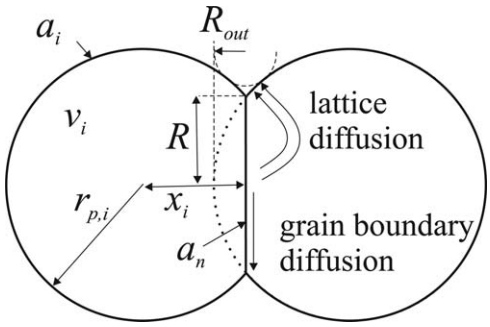


**Figure A1. A 2-D sketch of a pair of particles during sintering.**

**The atoms diffuse either along the grain boundary (grain boundary diffusion) or move through the crystal lattice into the neck (lattice or volume diffusion). For both mechanisms, the source of atoms is the grain boundary.[35]**

For lattice (volume) diffusion, the source of the atoms is the grain boundary as atoms move through the crystal lattice[35] to the particle surface so the volume of material transported through the neck area, $a_n = \pi R^2$, into the neck per time is

$$\frac{dv_p}{dt} = a_n \frac{dx_i}{dt} = J a_n \Omega \tag{A2}$$

where $v_p$ is the particle volume and $x$ is the particle center to neck distance. The concentration of lattice vacancies between the neck surface and neck center is assumed constant[35]: $dC_v/dR = \Delta C_v/R$, with

$$\Delta C_v = C_v - C_{v0} = C_{v0}\left(\exp\left(-\frac{\gamma\Omega}{k_B T}\left(\frac{1}{R_{out}} - \frac{1}{R}\right)\right) - 1\right) \tag{A3}$$

where $R_{out} = r_{p,i} - x_i$ is the outer neck radius,[30] $k_B$ the Boltzmann constant, $\gamma$ the surface energy, $T$ the temperature, and $C_{v0}$ the equilibrium vacancy concentration beneath a flat surface. Typically, $\gamma\Omega\left(\frac{1}{R_{out}} - \frac{1}{R}\right) \ll k_B T$,[40] except at the very beginning of sintering, when the outer neck radius is a few atom diameters. Then, the exponential function is approximated as $C_v = C_{v0}\left(1 - \frac{\gamma\Omega}{k_B T}\left(\frac{1}{R_{out}} - \frac{1}{R}\right)\right)$, which results in a vacancy concentration difference

$$\Delta C_v = -C_{v0}\frac{\gamma\Omega}{k_B T}\left(\frac{1}{R_{out}} - \frac{1}{R}\right) \tag{A4}$$

Equations A1 and A4 are substituted into Eq. A2 to determine the rate of shrinkage $dx_i/dt^*$

$$\frac{dx_i}{dt*} = -\frac{r_{p,0}^3}{R\pi}\left(\frac{1}{R_{out}} - \frac{1}{R}\right) \tag{7}$$

with the dimensionless time $t^* = t/\tau_0$

$$\tau_0 = \frac{k_B T r_{p,0}^3}{\pi D_v C_{v0}\gamma\Omega} \tag{9b}$$

where $r_{p,0}$ is the initial PP radius. The diffusion coefficient is expressed, at least over some limited temperature range, as a thermally activated process[40]

$$D_v = D_{v0}\exp\left(\frac{-Q}{N_A k_B T}\right) \tag{A5}$$

where $D_{v0}$ is a constant, $Q$ is an experimentally determined activation energy, and $N_A$ is the Avogadro number. Thus, the diffusion coefficient dominates the temperature dependence of $\tau_0$.

*Manuscript received Aug. 29, 2012, and revision received Dec. 21, 2012.*